ACS APPLIED NANO MATERIALS

www.acsanm.org Article

Large-Scale Vertical 1T′/2H $MoTe_2$ Nanosheet-Based Heterostructures for Low Contact Resistance Transistors

Shiqi Yang, Xiaolong Xu, Wanjin Xu, Bo Han, Zhengping Ding, Pingfan Gu, Peng Gao, and Yu Ye*

Cite This: *ACS Appl. Nano Mater.* 2020, 3, 10411−10417

Read Online

ACCESS | Metrics & More | Article Recommendations | Supporting Information

ABSTRACT: Because of atomic thickness and non-zero band gap, two-dimensional (2D) transition-metal dichalcogenides (TMDCs) have become promising candidates for post-silicon nanoelectronic materials. In the process of realizing 2D electronic devices for scaling down modern integrated circuitry, contact engineering suitable for large-scale manufacturing is crucial, but it remains elusive. Here, we demonstrated the large-scale chemical assembly of van der Waals heterostructures, with metallic 1T′-$MoTe_2$ on top of semiconducting 2H-$MoTe_2$, via a spatial-controlled phase-engineered growth method. Based on the heterophase structure, a large-scale field-effect transistor (FET) array was fabricated, in which 1T′-$MoTe_2$ was used as the contact electrode and 2H-$MoTe_2$ was used as the semiconducting channel. The vertical nanosheet-based heterophase FET exhibits ohmic contact behavior with distinctively low contact resistance. A total of 120 FETs were measured, and the measured average field-effect mobility was as high as 15 $cm^2 V^{-1} s^{-1}$ (comparable to that of exfoliated single-crystalline 2H-$MoTe_2$). The superior electrical properties are attributed to the atomic clean interface that leads to an ideal contact between top 1T′- and bottom 2H-$MoTe_2$. This spatially controlled large-scale chemical assembly of vertical 2D metal−semiconductor heterostructures with low contact resistance provides a new route toward the practical application of high-performance electronic and optoelectronic devices based on the atomically thin TMDCs.

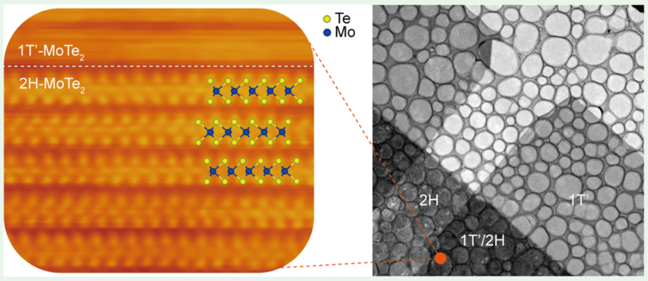

KEYWORDS: *$MoTe_2$, large-scale, chemical assembly, 1T′/2H heterophase, contact resistance*

INTRODUCTION

Because of the short-channel effect, scaling down the transistors for silicon-based integrated circuitry has encountered bottlenecks. For post-silicon nanoelectronics, two-dimensional (2D) semiconductors have become promising candidates because of their atomic thicknesses and non-zero band gaps.[1−9] In 2D short-channel electronics for scaling integrated circuits, the contact resistance is specifically important. However, the planar metal contacts to van der Waals (vdWs) semiconductors often suffer from unpredictable large contact resistance due to Fermi level pinning (FLP) between the metal and the 2D semiconductor.[10,11] In addition, direct deposition of metal electrodes on the surface of 2D semiconductors would cause considerable defects, strain, disorders, and metal diffusion, which are detrimental for the contact.[12]

Recently, great progress has been made in reducing the contact resistance of 2D semiconductors in contact with 2D metallic materials, which have two device configurations. One is the in-plane heterostructures (in-plane configuration) of 2D semiconductors and 2D metallic materials through coplanar contacts.[13−16] The other is the vertical contact of 2D semiconductors by 2D metallic materials through vdWs interface (vertical configuration).[17−20] The vertical configuration provides new opportunities for electronic and optoelectronic devices, for example, vertical field-effect transistor (FET).[21] Vertical 1T′/2H MoS_2 heterostructures have been demonstrated via the phase-controlled synthesis.[17] 2H-MoS_2 FETs with 1T′-MoS_2 contacts showed higher averaged mobility and lower contact resistance compared with metal-contacted 2H-MoS_2 channels. Similar results have also been observed in the heteroepitaxial vdWs contacts between single-layer metallic 1T′-WTe_2 and semiconducting 2H-WSe_2.[20] However, only a discrete and randomly distributed 2D metal−semiconductor heterophase structure can be obtained by these methods, which limits their application in the integrated ultrathin electronic circuitry. The wet transfer method was also used to construct large-scale $NbSe_2$/WSe_2 vertical heterostructures.[22] This inefficient wet transfer method cannot provide good spatial control and effectively locate the position of the semiconductor channels. Therefore, large-scale

Received: August 25, 2020
Accepted: September 11, 2020
Published: September 11, 2020

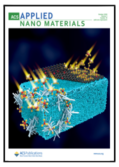

https://dx.doi.org/10.1021/acsanm.0c02302
ACS Appl. Nano Mater. 2020, 3, 10411−10417

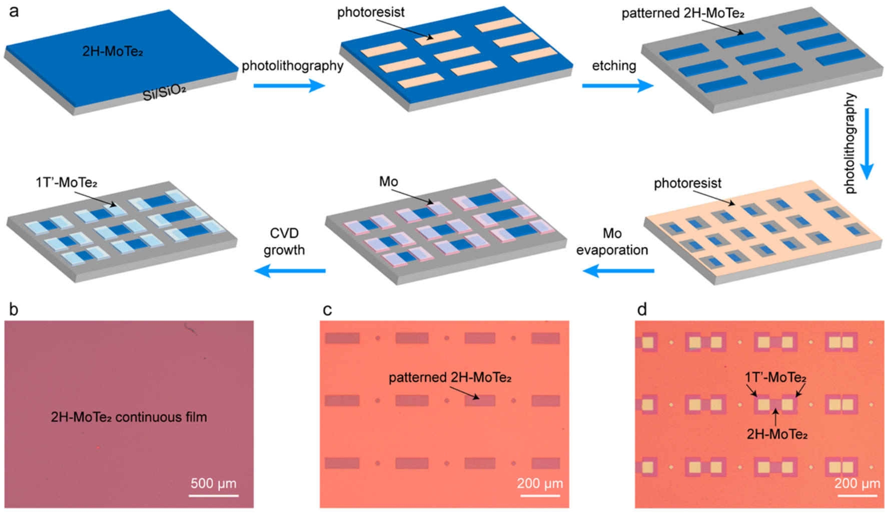

Figure 1. Schematic illustrations of the fabrication processes of the vertical 1T′/2H $MoTe_2$ heterophase array and corresponding optical images. (a) Fabrication processes of the vertical 1T′/2H $MoTe_2$ heterophase array. A continuous 2H-$MoTe_2$ film with a large domain size was first synthesized. After photolithography, RIE, and lift-off processes, the patterned 2H-$MoTe_2$ channel array was fabricated. Mo squares were prepared on both sides of the 2H-$MoTe_2$ channels and finally tellurized into 1T′-$MoTe_2$ after a low-temperature CVD growth. (b) Optical image of the 2H-$MoTe_2$ continuous film. (c) Optical image of the patterned 2H-$MoTe_2$ rectangle array. (d) Vertical 1T′/2H $MoTe_2$ heterophase array after the second CVD growth. The zoomed-out image of the vertical 1T′/2H $MoTe_2$ heterophase array with different channel lengths on a larger scale is shown in Figure S2.

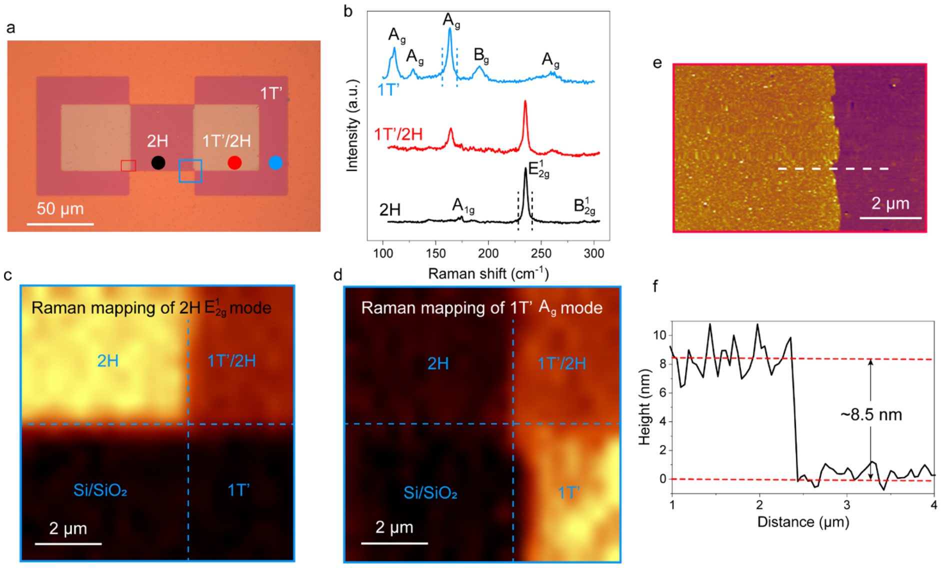

Figure 2. Raman and AFM characterizations of the vertical 1T′/2H $MoTe_2$ heterophase. (a) Optical image of a representative vertical 1T′/2H $MoTe_2$ heterophase structure. (b) Raman spectra of 1T′-, 2H-, and 1T′/2H $MoTe_2$ heterophase collected from the corresponding regions labeled in (a). (c,d) Raman mappings of the E^1_{2g} peak of 2H-$MoTe_2$ and the A_g peak of 1T′-$MoTe_2$ at the corresponding regions labeled in (a). (e) AFM height image at the 1T′/2H $MoTe_2$ heterophase boundary labeled in (a). (f) Height line profile along the white dashed line shown in (e) indicates that a 1T′-$MoTe_2$ layer was grown on top of 2H-$MoTe_2$ with a thickness of about 8.5 nm.

transfer-free chemical assembly of spatial-controlled vertical 2D metal−semiconductor heterostructures for 2D circuitry is still lacking.

The chemical assembly method is preferable because it keeps the promise for large-scale applications. Here, we demonstrated the large-scale chemical assembly of vertical vdWs 1T′/2H $MoTe_2$ (metal/semiconductor) heterostructures via a spatially controlled phase-engineering method, enabled by the small energy difference between 2H- and 1T′-$MoTe_2$ (∼40 meV per $MoTe_2$ formula unit).[23−27] The vertical 1T′/2H $MoTe_2$ nanosheet-based FETs exhibit ohmic contact behavior. The contact resistance and the average carrier mobility were extracted to be ∼36.4 kΩ μm (at a back-gate voltage of −90 V) and ∼15 $cm^2\ V^{-1}\ s^{-1}$, respectively, based on 120 measured FETs. Cross-sectional scanning transmission electron microscopy (STEM) was also performed to explore the atomic clean vdWs interface between top 1T′- and bottom 2H-$MoTe_2$. The close-to-perfect interface results in a low contact resistance contact for the high-performance devices, which is especially important in 2D electronic devices.[12,19] The large-scale chemical assembly method with interface contact engineering provides a new route for the realization of high-performance large-scale electronic and optoelectronic devices based on atomically thin $MoTe_2$.

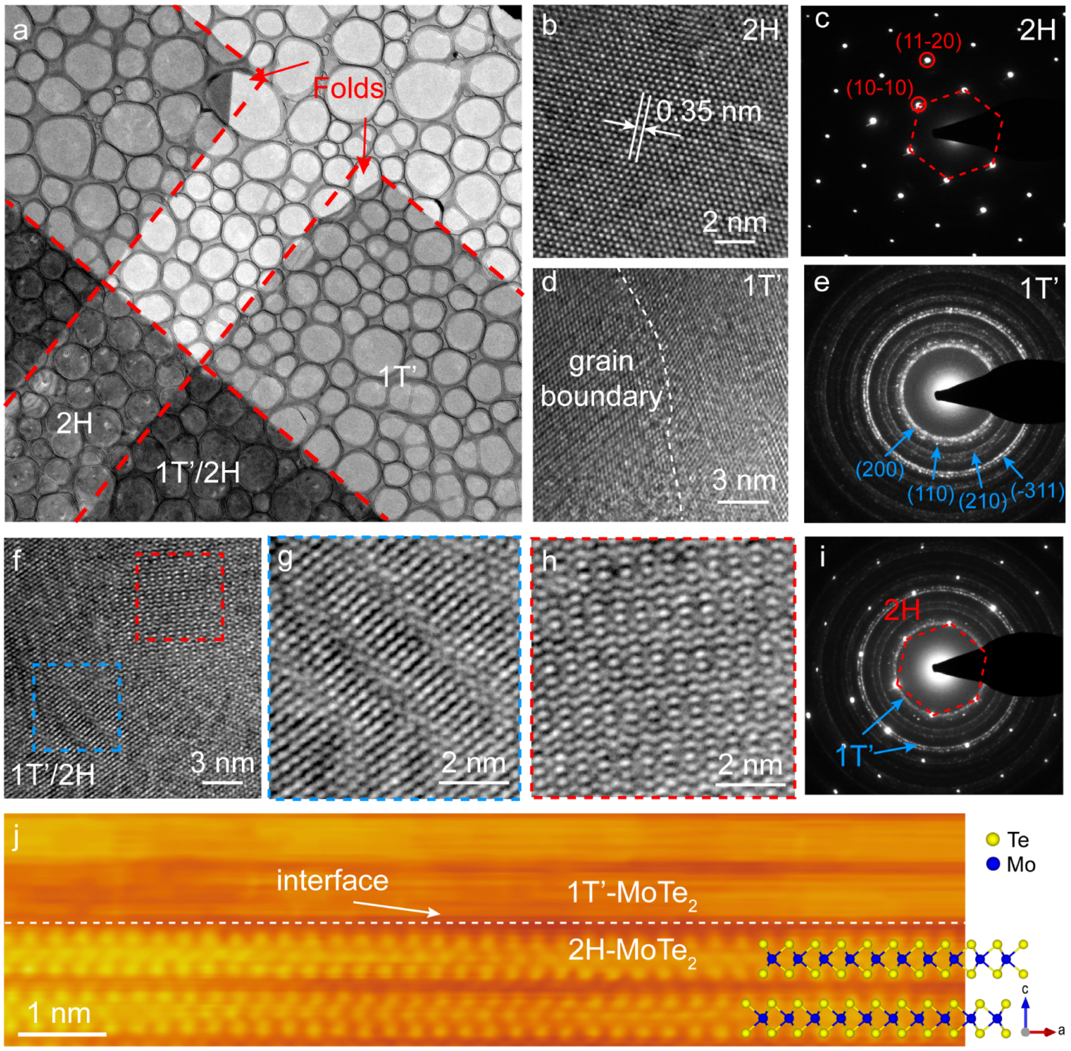

Figure 3. TEM characterizations of vertical 1T′/2H $MoTe_2$ heterophase. (a) Low-magnification BF-TEM image of the vertical 1T′/2H $MoTe_2$ heterophase structure. (b) HR-TEM image of the 2H-$MoTe_2$ region, indicating a hexagonal structure. (c) SAED pattern of the 2H-$MoTe_2$ region with an aperture size of 800 nm, showing a single set of six-fold symmetric diffraction spots. (d) HR-TEM image of the 1T′-$MoTe_2$ region. The white dashed line indicates the grain boundary between two different 1T′-$MoTe_2$ domains. (e) SAED pattern of the 1T′-$MoTe_2$ region shows several diffraction rings, indicative of the polycrystalline nature. (f) HR-TEM image of the vertical 1T′/2H $MoTe_2$ heterophase region. (g,h) Zoomed-in HR-TEM images from different heterophase regions, showing different periodic Moiré patterns. (i) SAED pattern of the heterophase region contains a set of six-fold symmetric diffraction from 2H-$MoTe_2$ and several diffraction rings from the 1T′-$MoTe_2$. (j) Atomic-resolution cross-sectional HAADF-STEM image of the vertical 1T′/2H $MoTe_2$ with the corresponding atomic model for 2H-$MoTe_2$.

■ RESULTS AND DISCUSSION

Figure 1a illustrates the fabrication process of the vertical 1T′/2H $MoTe_2$ heterophase array. First, the large-area continuous 2H-$MoTe_2$ film with a large domain size (hundreds of micrometers in diameter) was synthesized using a chemical vapor deposition (CVD) method.[28,29] In short, first, molybdenum (Mo) thin films with 2 nm thickness were prepared by magnetron sputtering on a Si/SiO_2 substrate. Then, the 2H-$MoTe_2$ film was acquired by tellurization of the Mo film at 640 °C for 2 h. In the tellurization process, polycrystalline 1T′-$MoTe_2$ film with Te vacancies was first obtained. Then, randomly distributed 2H-$MoTe_2$ domains nucleated and grew via the phase transition process until they finally merged together, forming a high-quality continuous 2H-$MoTe_2$ film.[28] The synthesized $MoTe_2$ film showed a homogeneous optical contrast (Figure 1b), which indicated a uniform sample thickness. Topographic atomic force microscopy (AFM) image recorded in the 2H-$MoTe_2$ film reveals a uniformity in its surface morphology (Figure S1a). The height line profile of 2H-$MoTe_2$ showed a thickness of ∼5 nm, corresponding to seven-layer $MoTe_2$ (Figure S1b).[29] The 2H-$MoTe_2$ film on the Si/SiO_2 substrate was then patterned into rectangular shapes by conventional photolithography, followed by Ar and SF_6 plasma reactive ion etching (RIE) and lift-off processes (Figure 1c). To assemble the spatially controlled metallic 1T′-$MoTe_2$ contact electrodes, a Mo film (4 nm thick) was deposited on both sides of 2H-$MoTe_2$ with different channel lengths by conventional photolithography. The sample was then sent back to the furnace where the Mo film was tellurized into 1T′-$MoTe_2$ at a temperature of 530 °C for 30 min. Under this low-temperature growth, no 2H-$MoTe_2$ nucleation was formed, and the original 2H-$MoTe_2$ channels remain unaffected, giving rise to the large-scale vertical 1T′/2H $MoTe_2$ heterophase array (Figure 1d).

Raman spectroscopy was employed to characterize the 2H-$MoTe_2$, vertical 1T′/2H $MoTe_2$, and 1T′-$MoTe_2$ regions

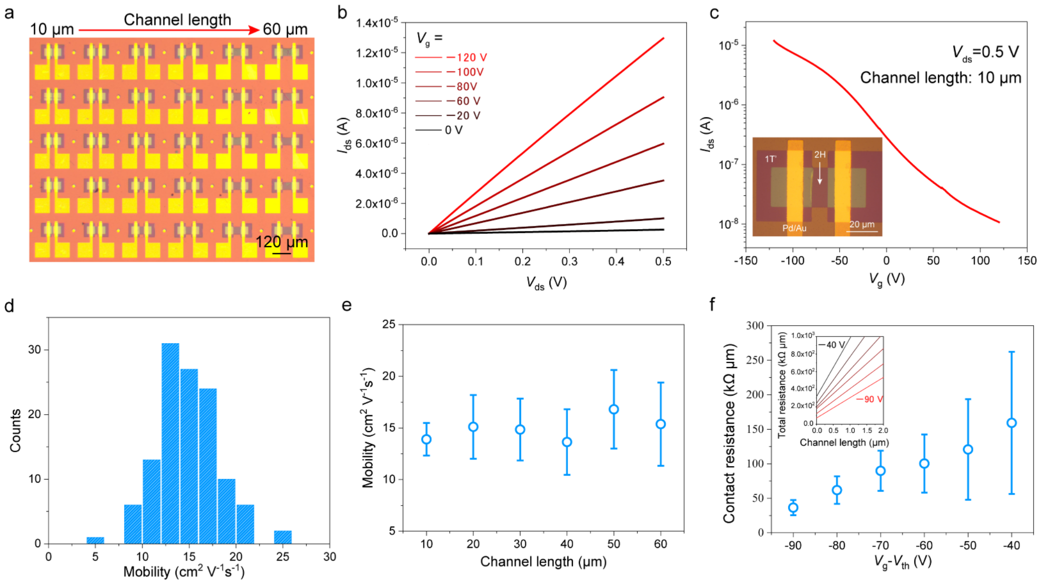

Figure 4. Electrical characterizations of the 1T′/2H $MoTe_2$ heterophase-contacted FETs at room temperature. (a) Optical image of the large-scale 1T′/2H $MoTe_2$ heterophase-based FET array. (b) Typical I_{ds} vs V_{ds} curves measured at different back-gate voltages from −120 to 0 V, which all show linear characteristics indicating an ohmic contact. (c) Room-temperature field-effect transfer curve at a bias voltage of 0.5 V. The 2H-$MoTe_2$ channel shows p-type characteristics with an on−off ratio of ∼10^3. (d) Histogram statistics of the field-effect mobility extracted from 120 FETs, showing an average mobility of ∼15 cm^2 V^{-1} s^{-1}. (e) Measured field-effect mobility with channel length from 10 to 60 μm, showing that the mobility is independent of the channel length. The error bars in (e,f) are calculated from the sample to sample variations. (f) Contact resistance of 1T′/2H $MoTe_2$ as a function of the back-gate voltage extracted from the TLM. The inset shows the total contact resistance vs channel length under different back-gate voltages.

(labeled in Figure 2a). The channel is confirmed to be 2H-$MoTe_2$ by the appearance of the well-resolved out-of-plane A_{1g} (171 cm^{-1}), B^1_{2g} (291 cm^{-1}) and in-plane E^1_{2g} (234 cm^{-1}) Raman signatures of 2H-$MoTe_2$ (Figure 2b). The region that does not overlap with 2H-$MoTe_2$ is identified to be 1T′-$MoTe_2$ by the presence of the typical A_g Raman modes (107, 127, 161, and 256 cm^{-1}) of 1T′-$MoTe_2$.[30,31] In the overlapped region, we can observe both the 1T′-$MoTe_2$ A_g Raman mode (161 cm^{-1}) and the 2H-$MoTe_2$ E^1_{2g} (234 cm^{-1}) Raman mode. Raman mapping of the 2H-$MoTe_2$ E^1_{2g} (234 cm^{-1}) peak (Figure 2c) shows uniform signals in the 2H and heterophase regions, respectively, while Raman mapping of the 1T′-$MoTe_2$ A_g (161 cm^{-1}) peak (Figure 2d) shows uniform signals in the 1T′ and heterophase regions, respectively, with clear and distinct interfaces. It is noticeable that the Raman intensities of both 1T′- and 2H-$MoTe_2$ are weak in the vertical heterophase region, which might result from the low collection efficiency of the Raman scattering signal with the appearance of the adhesion layer.[5] AFM height image across the interface between the 2H-$MoTe_2$ channel and the heterophase contact region (labeled in Figure 2a) exhibited a homogeneous contrast (Figure 2e) with a ∼8.5 nm step (Figure 2f), indicating the formation of a uniform 1T′-$MoTe_2$ layer on top of 2H-$MoTe_2$.

The vertical 1T′/2H $MoTe_2$ heterophase array was transferred onto a copper microgrid to further evaluate the crystallinity (see details in the Supporting Information Figure S3). From the low-magnification bright-field (BF) transmission electron microscopy (TEM) image (Figure 3a), we can identify three typical regions as 2H-$MoTe_2$, 1T′-$MoTe_2$, and 1T′/2H $MoTe_2$ heterophase. Some folds appeared at the corners of 1T′-$MoTe_2$ (indicated by arrows in Figure 3a), which might occur during the wet transfer process. From the high-resolution TEM (HR-TEM) image (Figure 3b), it can be seen that 2H-$MoTe_2$ shows a hexagonal structure with a spacing distance of 0.35 nm (Figure 3b).[32] The corresponding selected area electron diffraction (SAED) pattern recorded in the 2H region with an aperture of 800 nm in diameter shows a single set of six-fold symmetric diffraction spots (Figure 3c), indicating the single-crystal nature. In contrast, the HR-TEM image of the 1T′-$MoTe_2$ region (Figure 3d) shows a monoclinic structure with a domain size of about tens of nanometers, indicating the polycrystalline nature (low-magnification BF-TEM image in the Supporting Information Figure S4). The SAED pattern from the 1T′ phase region shows several diffraction rings, again indicating the polycrystalline nature of the 1T′-$MoTe_2$ film (Figure 3e). The polycrystalline 1T′-$MoTe_2$ film is textured in the [001] direction (Figure 3e).[33]

At the 1T′/2H heterophase region, the Moiré patterns occur when the monoclinic 1T′-$MoTe_2$ was grown on top of the hexagonal 2H-$MoTe_2$ with rotation angles respect to each other (Figure 3f). Since 1T′-$MoTe_2$ is polycrystalline with domain sizes of tens of nanometers, different Moiré patterns can be observed in different heterophase regions (Figure 3g,h; see more different Moiré patterns in Figure S5). The SAED pattern of the vertical 1T′/2H $MoTe_2$ region contains a set of six-fold symmetric diffraction spots from 2H-$MoTe_2$ and several diffraction rings from 1T′-$MoTe_2$, confirming the heterophase structure (Figure 3i).

To further identify the vdWs contact at the 1T′/2H $MoTe_2$ heterophase region, we performed cross-sectional STEM. From the high-angle annular dark-field STEM (HAADF-STEM) of the contact region (Figure 3j), we can see that the few-layer 1T′-$MoTe_2$ stacks on the few-layer 2H-$MoTe_2$ without any atomic intermixing or damages. A clean vdWs gap is observed between the top 1T′-$MoTe_2$ and bottom 2H-$MoTe_2$ with a distance of ∼0.65 nm. Because of the random crystalline orientation of 1T′-MoTe$_2$ respect to that of 2H-MoTe$_2$, the atomic structure of 1T′-MoTe$_2$ is not well resolved in the HAADF-STEM image. Coupled with the well-resolved Moiré patterns in the top view of the heterostructure, we conclude that an atomically clean vdWs interface is formed between the contact of 1T′-MoTe$_2$ and 2H-MoTe$_2$.

To explore the electrical characteristics of the vertical 1T′/2H MoTe$_2$ heterophase array, Pd/Au (10/50 nm) electrodes were deposited on the 1T′-MoTe$_2$ contact for the external connections (Figure 4a). The heavily doped Si substrate was used as the back-gate electrode. The 2H-MoTe$_2$ FET directly contacted with Pd/Au electrodes was also fabricated for comparison (Figure S6a). With the same channel length, the FET with the heterophase contact (Figure 4c) exhibits a higher on-current than the FET that directly contacted by the Pd/Au metal electrodes (Figure S6b). The typical source-drain current−voltage (I_{ds}−V_{ds}) curves of the FET with a channel length of 10 μm measured at multiple gate voltages from −120 to 0 V all show linear behaviors, indicating the ohmic contact of the vertical 1T′/2H MoTe$_2$ heterophase (Figure 4b). The measured I_{ds} versus gate voltages (V_g) of the heterophase FET shows p-type channel characteristics with an on−off ratio of ∼1 × 10^3 (Figure 4c). The field-effect mobility, $\mu = (dI_{ds}/dV_g)(L/W)(1/V_{ds}C_g)$, where L, W, and C_g are the channel length, channel width, and the gate capacitance per unit area, respectively, was measured to be ∼18 cm^2 V^{-1} s^{-1} at room temperature. In contrast, the field-effect mobility measured from the direct metal contacted 2H-MoTe$_2$ FET is only ∼2 cm^2 V^{-1} s^{-1} (Figure S6b).

We measured 120 FETs with different channel lengths (from 10 to 60 μm) in total and found that the mobility of the 1T′/2H MoTe$_2$ heterophase-contacted FETs showed a Gaussian distribution with an average mobility of 15 cm^2 V^{-1} s^{-1} (Figure 4d), which is comparable to the previously reported values from the exfoliated single-crystal 2H-MoTe$_2$ channels.[34] In addition, the field-effect mobilities of different channel lengths have similar values of 10−20 cm^2 V^{-1} s^{-1} (Figure 4e, see detailed mobility distributions vs different channel lengths in Supporting Information Figure S7), probably attributed to the large 2H-MoTe$_2$ single-crystalline domain size.[28] Compared with some recently reported works based on MoTe$_2$ (including both in-plane and vertical configurations), considering field-effect mobility, integration level, on−off ratio, and so forth (details are shown in Supporting Information Table S1), our 1T′/2H MoTe$_2$ heterophase-contacted FETs show superior device properties in general.

To further extract the contact resistance R_c of the heterophase structure, transfer length method (TLM) was used to obtain the length-dependent resistance in both 1T′/2H MoTe$_2$ FET and 1T′-MoTe$_2$ samples.[13,28] The total R_c of the metal/1T′/2H MoTe$_2$ structure contains R_c between the metal and 1T′-MoTe$_2$ and R_c between 1T′- and 2H-MoTe$_2$. Because of the semiconducting property of 2H-MoTe$_2$, the total R_c (metal/1T′/2H MoTe$_2$) strongly depends on the back-gate voltage. The minimum total R_c was measured to be ∼36.4 kΩ μm at a high doping level (inset of Figure 4f). The R_c between the Pd/Au electrode and the 1T′-MoTe$_2$ film was measured to be 0.8 kΩ μm (Figure S8b), independent of the gate voltage due to the metallic property of 1T′-MoTe$_2$, which is confirmed by the low-temperature transport measurements (Figure S8c). Therefore, the R_c between 1T′- and 2H-MoTe$_2$ is ∼35.6 kΩ μm at the high doping level. The contact resistance is reduced by more than 1 order of magnitude compared with that of metal-contacted 2H-MoTe$_2$ (reported value of 409 kΩ μm).[16] The contact of this vertical 1T′/2H MoTe$_2$ heterostructure does not show superior characteristics to that of our previously reported in-plane 1T′/2H MoTe$_2$ heterostructures,[28] which may be attributed to the tunnel barrier originating from the small vdWs gap at the interface (Figure S9).[11]

Confirmed by the cross-sectional HAADF-STEM image (Figure 3j), this clean vdWs interface of 1T′/2H MoTe$_2$ heterostructures could eliminate the FLP effect and lead to a contact approaching the ideal physical model.[12] The Kelvin probe force microscopy results show that our 1T′-MoTe$_2$ has a higher work function than 2H-MoTe$_2$,[28] which is suitable for the ohmic contact between the p-type 2H-MoTe$_2$ and metallic 1T′-MoTe$_2$, leading to low contact resistance and improved field-effect mobility. Moreover, the chemical assembly method also keeps the promise for large-scale applications.

■ CONCLUSIONS

In summary, we demonstrated a large-scale chemical assembly of vdWs integration of vertical metallic and semiconducting MoTe$_2$ heterophase with spatial-controlled capability. The nanosheet-based heterophase contacts exhibited lower contact resistance and efficient carrier injection because of the perfect interface, thus showing superior FET characteristics compared to those of the conventional metal contacted transistors. This spatial-controlled vertical contact engineering with 1T′-MoTe$_2$ and 2H-MoTe$_2$ on a large scale provides new route toward the practical application of MoTe$_2$ nanosheet-based devices with low contact resistance in electronics and optoelectronics.

■ METHODS

Synthesis of 1T′- and 2H-MoTe$_2$. The synthesis of the MoTe$_2$ films was conducted via a CVD method by tellurizing the Mo films at different temperatures. The detailed information of the synthesis processes can be found in our previously published work.[28]

Fabrication of 1T′/2H MoTe$_2$ Heterostructure-Based FET Array. First, the 2H-MoTe$_2$ film was acquired by tellurizing the Mo film at 640 °C for 2 h. Then, the continuous 2H-MoTe$_2$ film was patterned into rectangular shapes by conventional photolithography, followed by Ar and SF$_6$ plasma RIE and lift-off processes. Then, another photolithography process was used to define the contact regions on both sides of each 2H channel, followed by the deposition of 5 nm Mo film and the lift-off process. The substrates were then returned into the furnace, and the contact regions were tellurized to 1T′-MoTe$_2$ film at 530 °C for 30 min. At this low temperature, no 2H-MoTe$_2$ nucleation was formed and the original 2H-MoTe$_2$ channels remain unaffected, resulting in the large-scale 1T′/2H MoTe$_2$ heterophase FET array. For the electrical characterizations, Pd/Au (10/70 nm) electrodes were defined on the 1T′ MoTe$_2$ regions for external wire bonding. The 1T′/2H MoTe$_2$ heterophase arrays were transferred onto the copper grids for further TEM characterization.

Transfer of 1T′/2H/1T′ MoTe$_2$ Heterophase Array. Wet transfer method was used to prepare the 1T′/2H/1T′ MoTe$_2$ heterophase array sample for TEM characterizations, and the detailed transfer processes are provided in Supporting Information Figure S3.

Raman Spectroscopy of 1T′-, 2H-, and 1T′/2H MoTe$_2$ Heterophase. Raman spectra of 1T′-, 2H-, and 1T′/2H MoTe$_2$ heterophase regions were collected using the WITec alpha300 confocal innovation system. The XYZ piezo-scan stage is equipped to automatically scan the sample. A 532 nm laser was used as the excitation laser source and was focused by a 50× (0.55 NA, Zeiss) objective. Raman signals were collected by the same objective and were detected using a spectrograph with 1800 g/mm grating coupled with a charged coupled device. Raman mapping was performed on the 1T′-, 2H-, and 1T′/2H $MoTe_2$ heterophase regions. The integrated Raman intensities of the 2H-$MoTe_2$ E^1_{2g} peak and the 1T′-$MoTe_2$ A_g peak were used to generate the Raman intensity maps, respectively.

■ ASSOCIATED CONTENT

Supporting Information

The Supporting Information is available free of charge at https://pubs.acs.org/doi/10.1021/acsanm.0c02302.

> AFM measurement of 2H-$MoTe_2$ film; patterned growth of 1T′-$MoTe_2$; transfer of the 1T′/2H/1T′ $MoTe_2$ heterophase array; TEM characterization of the 1T′-$MoTe_2$ region and the 1T′/2H $MoTe_2$ heterophase region; metal/2H-$MoTe_2$ contact for comparison; detailed calculation and results for field-effect mobility; resistance of metal/1T′-$MoTe_2$ contact; band diagram comparison of the vertical contact and in-plane contact; and comparison with other reported works (PDF)

■ AUTHOR INFORMATION

Corresponding Author

Yu Ye − *State Key Laboratory for Mesoscopic Physics and Frontiers Science Center for Nano-optoelectronics, School of Physics, Peking University, Beijing 100871, China; Collaborative Innovation Center of Quantum Matter, Beijing 100871, China; Peking University Yangtze Delta Institute of Optoelectronics, Nantong 226010, Jiangsu, China;* orcid.org/0000-0001-6046-063X; Email: ye_yu@pku.edu.cn

Authors

Shiqi Yang − *State Key Laboratory for Mesoscopic Physics and Frontiers Science Center for Nano-optoelectronics, School of Physics and Academy for Advanced Interdisciplinary Studies, Peking University, Beijing 100871, China*

Xiaolong Xu − *State Key Laboratory for Mesoscopic Physics and Frontiers Science Center for Nano-optoelectronics, School of Physics, Peking University, Beijing 100871, China*

Wanjin Xu − *State Key Laboratory for Mesoscopic Physics and Frontiers Science Center for Nano-optoelectronics, School of Physics, Peking University, Beijing 100871, China*

Bo Han − *Electron Microscopy Laboratory, School of Physics, Peking University, Beijing 100871, China*

Zhengping Ding − *Electron Microscopy Laboratory, School of Physics, Peking University, Beijing 100871, China;* orcid.org/0000-0001-5275-5905

Pingfan Gu − *State Key Laboratory for Mesoscopic Physics and Frontiers Science Center for Nano-optoelectronics, School of Physics, Peking University, Beijing 100871, China*

Peng Gao − *Collaborative Innovation Center of Quantum Matter, Beijing 100871, China; Electron Microscopy Laboratory, School of Physics and International Center for Quantum Materials, School of Physics, Peking University, Beijing 100871, China;* orcid.org/0000-0003-0860-5525

Complete contact information is available at: https://pubs.acs.org/10.1021/acsanm.0c02302

Notes

The authors declare no competing financial interest.

■ ACKNOWLEDGMENTS

This work was supported by the Beijing Natural Science Foundation (4182028), Key Research Program of Frontier Sciences, CAS (grant no. ZDBS-LY-JSC015), the National Key R&D Program of China (grant no. 2018YFA0306900), and the National Natural Science Foundation of China (grant no. 6152004).

■ REFERENCES

(1) Wang, Q. H.; Kalantar-Zadeh, K.; Kis, A.; Coleman, J. N.; Strano, M. S. Electronics and optoelectronics of two-dimensional transition metal dichalcogenides. *Nat. Nanotechnol.* **2012**, *7*, 699−712.

(2) Lin, Z.; Liu, Y.; Halim, U.; Ding, M.; Liu, Y.; Wang, Y.; Jia, C.; Chen, P.; Duan, X.; Wang, C.; Song, F.; Li, M.; Wan, C.; Huang, Y.; Duan, X. Solution-processable 2D semiconductors for high-performance large-area electronics. *Nature* **2018**, *562*, 254−258.

(3) Kang, K.; Lee, K.-H.; Han, Y.; Gao, H.; Xie, S.; Muller, D. A.; Park, J. Layer-by-layer assembly of two-dimensional materials into wafer-scale heterostructures. *Nature* **2017**, *550*, 229−233.

(4) Yu, H.; Liao, M.; Zhao, W.; Liu, G.; Zhou, X. J.; Wei, Z.; Xu, X.; Liu, K.; Hu, Z.; Deng, K.; Zhou, S.; Shi, J.-A.; Gu, L.; Shen, C.; Zhang, T.; Du, L.; Xie, L.; Zhu, J.; Chen, W.; Yang, R.; Shi, D.; Zhang, G. Wafer-Scale Growth and Transfer of Highly-Oriented Monolayer MoS_2 Continuous Films. *ACS Nano* **2017**, *11*, 12001−12007.

(5) Xue, Y.; Zhang, Y.; Liu, Y.; Liu, H.; Song, J.; Sophia, J.; Liu, J.; Xu, Z.; Xu, Q.; Wang, Z.; Zheng, J.; Liu, Y.; Li, S.; Bao, Q. Scalable Production of a Few-Layer MoS_2/WS_2 Vertical Heterojunction Array and Its Application for Photodetectors. *ACS Nano* **2016**, *10*, 573−580.

(6) Li, L.; Yang, F.; Ye, G. J.; Zhang, Z.; Zhu, Z.; Lou, W.; Zhou, X.; Li, L.; Watanabe, K.; Taniguchi, T.; Chang, K.; Wang, Y.; Chen, X. H.; Zhang, Y. Quantum Hall effect in black phosphorus two-dimensional electron system. *Nat. Nanotechnol.* **2016**, *11*, 593−597.

(7) Bandurin, D. A.; Tyurnina, A. V.; Yu, G. L.; Mishchenko, A.; Zólyomi, V.; Morozov, S. V.; Kumar, R. K.; Gorbachev, R. V.; Kudrynskyi, Z. R.; Pezzini, S.; Kovalyuk, Z. D.; Zeitler, U.; Novoselov, K. S.; Patanè, A.; Eaves, L.; Grigorieva, I. V.; Fal'ko, V. I.; Geim, A. K.; Cao, Y. High electron mobility, quantum Hall effect and anomalous optical response in atomically thin InSe. *Nat. Nanotechnol.* **2016**, *12*, 223−227.

(8) Qiu, G.; Wang, Y.; Nie, Y.; Zheng, Y.; Cho, K.; Wu, W.; Ye, P. D. Quantum Transport and Band Structure Evolution under High Magnetic Field in Few-Layer Tellurene. *Nano Lett.* **2018**, *18*, 5760−5767.

(9) Yuan, K.; Yin, R.; Li, X.; Han, Y.; Wu, M.; Chen, S.; Liu, S.; Xu, X.; Watanabe, K.; Taniguchi, T.; Muller, D. A.; Shi, J.; Gao, P.; Wu, X.; Ye, Y.; Dai, L. Realization of Quantum Hall Effect in Chemically Synthesized InSe. *Adv. Funct. Mater.* **2019**, *29*, 1904032.

(10) English, C. D.; Shine, G.; Dorgan, V. E.; Saraswat, K. C.; Pop, E. Improved Contacts to MoS_2 Transistors by Ultra-High Vacuum Metal Deposition. *Nano Lett.* **2016**, *16*, 3824−3830.

(11) Allain, A.; Kang, J.; Banerjee, K.; Kis, A. Electrical contacts to two-dimensional semiconductors. *Nat. Mater.* **2015**, *14*, 1195−1205.

(12) Liu, Y.; Guo, J.; Zhu, E.; Liao, L.; Lee, S.-J.; Ding, M.; Shakir, I.; Gambin, V.; Huang, Y.; Duan, X. Approaching the Schottky−Mott limit in van der Waals metal−semiconductor junctions. *Nature* **2018**, *557*, 696−700.

(13) Xu, X.; Liu, S.; Han, B.; Han, Y.; Yuan, K.; Xu, W.; Yao, X.; Li, P.; Yang, S.; Gong, W.; Muller, D. A.; Gao, P.; Ye, Y.; Dai, L. Scaling-up Atomically Thin Coplanar Semiconductor−Metal Circuitry via Phase Engineered Chemical Assembly. *Nano Lett.* **2019**, *19*, 6845−6852.

(14) Cho, S.; Kim, S.; Kim, J. H.; Zhao, J.; Seok, J.; Keum, D. H.; Baik, J.; Choe, D.-H.; Chang, K. J.; Suenaga, K.; Kim, S. W.; Lee, Y. H.; Yang, H. Phase patterning for ohmic homojunction contact in $MoTe_2$. *Science* **2015**, *349*, 625−628.

(15) Sung, J. H.; Heo, H.; Si, S.; Kim, Y. H.; Noh, H. R.; Song, K.; Kim, J.; Lee, C.-S.; Seo, S.-Y.; Kim, D.-H.; Kim, H. K.; Yeom, H. W.;

Kim, T.-H.; Choi, S.-Y.; Kim, J. S.; Jo, M.-H. Coplanar semiconductor−metal circuitry defined on few-layer $MoTe_2$ via polymorphic heteroepitaxy. *Nat. Nanotechnol.* **2017**, *12*, 1064.

(16) Kappera, R.; Voiry, D.; Yalcin, S. E.; Branch, B.; Gupta, G.; Mohite, A. D.; Chhowalla, M. Phase-engineered low-resistance contacts for ultrathin MoS_2 transistors. *Nat. Mater.* **2014**, *13*, 1128−1134.

(17) Liu, L.; Wu, J.; Wu, L.; Ye, M.; Liu, X.; Wang, Q.; Hou, S.; Lu, P.; Sun, L.; Zheng, J.; Xing, L.; Gu, L.; Jiang, X.; Xie, L.; Jiao, L. Phase-selective synthesis of 1T′ MoS_2 monolayers and heterophase bilayers. *Nat. Mater.* **2018**, *17*, 1108−1114.

(18) Tang, H.-L.; Chiu, M.-H.; Tseng, C.-C.; Yang, S.-H.; Hou, K.-J.; Wei, S.-Y.; Huang, J.-K.; Lin, Y.-F.; Lien, C.-H.; Li, L.-J. Multilayer Graphene−WSe_2 Heterostructures for WSe_2 Transistors. *ACS Nano* **2017**, *11*, 12817−12823.

(19) Wang, Y.; Kim, J. C.; Wu, R. J.; Martinez, J.; Song, X.; Yang, J.; Zhao, F.; Mkhoyan, A.; Jeong, H. Y.; Chhowalla, M. Van der Waals contacts between three-dimensional metals and two-dimensional semiconductors. *Nature* **2019**, *568*, 70−74.

(20) Lee, C.-S.; Oh, S. J.; Heo, H.; Seo, S.-Y.; Kim, J.; Kim, Y. H.; Kim, D.; Ngome Okello, O. F.; Shin, H.; Sung, J. H.; Choi, S.-Y.; Kim, J. S.; Kim, J. K.; Jo, M.-H. Epitaxial van der Waals Contacts between Transition-Metal Dichalcogenide Monolayer Polymorphs. *Nano Lett.* **2019**, *19*, 1814−1820.

(21) Yu, W. J.; Li, Z.; Zhou, H.; Chen, Y.; Wang, Y.; Huang, Y.; Duan, X. Vertically stacked multi-heterostructures of layered materials for logic transistors and complementary inverters. *Nat. Mater.* **2013**, *12*, 246−252.

(22) Kim, A. R.; Kim, Y.; Nam, J.; Chung, H.-S.; Kim, D. J.; Kwon, J.-D.; Park, S. W.; Park, J.; Choi, S. Y.; Lee, B. H.; Park, J. H.; Lee, K. H.; Kim, D.-H.; Choi, S. M.; Ajayan, P. M.; Hahm, M. G.; Cho, B. Alloyed 2D Metal−Semiconductor Atomic Layer Junctions. *Nano Lett.* **2016**, *16*, 1890−1895.

(23) Cho, S.; Kim, S.; Kim, J. H.; Zhao, J.; Seok, J.; Keum, D. H.; Baik, J.; Choe, D.-H.; Chang, K. J.; Suenaga, K.; Kim, S. W.; Lee, Y. H.; Yang, H. Phase patterning for ohmic homojunction contact in $MoTe_2$. *Science* **2015**, *349*, 625−628.

(24) Duerloo, K.-A. N.; Li, Y.; Reed, E. J. Structural phase transitions in two-dimensional Mo- and W-dichalcogenide monolayers. *Nat. Commun.* **2014**, *5*, 4214.

(25) Li, Y.; Duerloo, K.-A. N.; Wauson, K.; Reed, E. J. Structural semiconductor-to-semimetal phase transition in two-dimensional materials induced by electrostatic gating. *Nat. Commun.* **2016**, *7*, 10671.

(26) Song, S.; Keum, D. H.; Cho, S.; Perello, D.; Kim, Y.; Lee, Y. H. Room Temperature Semiconductor−Metal Transition of $MoTe_2$ Thin Films Engineered by Strain. *Nano Lett.* **2016**, *16*, 188−193.

(27) Keum, D. H.; Cho, S.; Kim, J. H.; Choe, D.-H.; Sung, H.-J.; Kan, M.; Kang, H.; Hwang, J.-Y.; Kim, S. W.; Yang, H.; Chang, K. J.; Lee, Y. H. Bandgap opening in few-layered monoclinic $MoTe_2$. *Nat. Phys.* **2015**, *11*, 482−486.

(28) Xu, X.; Chen, S.; Liu, S.; Cheng, X.; Xu, W.; Li, P.; Wan, Y.; Yang, S.; Gong, W.; Yuan, K.; Gao, P.; Ye, Y.; Dai, L. Millimeter-Scale Single-Crystalline Semiconducting $MoTe_2$ via Solid-to-Solid Phase Transformation. *J. Am. Chem. Soc.* **2019**, *141*, 2128−2134.

(29) Zhou, L.; Xu, K.; Zubair, A.; Liao, A. D.; Fang, W.; Ouyang, F.; Lee, Y.-H.; Ueno, K.; Saito, R.; Palacios, T.; Kong, J.; Dresselhaus, M. S. Large-Area Synthesis of High-Quality Uniform Few-Layer $MoTe_2$. *J. Am. Chem. Soc.* **2015**, *137*, 11892−11895.

(30) Yamamoto, M.; Wang, S. T.; Ni, M.; Lin, Y.-F.; Li, S.-L.; Aikawa, S.; Jian, W.-B.; Ueno, K.; Wakabayashi, K.; Tsukagoshi, K. Strong Enhancement of Raman Scattering from a Bulk-Inactive Vibrational Mode in Few-Layer $MoTe_2$. *ACS Nano* **2014**, *8*, 3895−3903.

(31) Ma, X.; Guo, P.; Yi, C.; Yu, Q.; Zhang, A.; Ji, J.; Tian, Y.; Jin, F.; Wang, Y.; Liu, K.; Xia, T.; Shi, Y.; Zhang, Q. Raman scattering in the transition-metal dichalcogenides of 1T′−$MoTe_2$,Td−$MoTe_2$, and Td−WTe_2. *Phys. Rev. B* **2016**, *94*, 214105.

(32) Ma, R.; Zhang, H.; Yoo, Y.; Degregorio, Z. P.; Jin, L.; Golani, P.; Ghasemi Azadani, J.; Low, T.; Johns, J. E.; Bendersky, L. A.; Davydov, A. V.; Koester, S. J. $MoTe_2$ Lateral Homojunction Field-Effect Transistors Fabricated using Flux-Controlled Phase Engineering. *ACS Nano* **2019**, *13*, 8035−8046.

(33) Naylor, C. H.; Parkin, W. M.; Ping, J.; Gao, Z.; Zhou, Y. R.; Kim, Y.; Streller, F.; Carpick, R. W.; Rappe, A. M.; Drndić, M.; Kikkawa, J. M.; Johnson, A. T. C. Monolayer Single-Crystal 1T'-$MoTe_2$ Grown by Chemical Vapor Deposition Exhibits Weak Antilocalization Effect. *Nano Lett.* **2016**, *16*, 4297−4304.

(34) Pradhan, N. R.; Rhodes, D.; Feng, S.; Xin, Y.; Memaran, S.; Moon, B.-H.; Terrones, H.; Terrones, M.; Balicas, L. Field-Effect Transistors Based on Few-Layered α-$MoTe_2$. *ACS Nano* **2014**, *8*, 5911−5920.